JoT JOURNAL OF TURBULENCE

http://jot.iop.org/

Effects of coastal geometry and the formation of cyclonic/anti-cyclonic eddies on turbulent mixing in upwelling simulation†

Yu-Heng Tseng and Joel H Ferziger

Environmental Fluid Mechanics Laboratory, Stanford University, Stanford, CA 94305-4020, USA
E-mail: yhtseng@stanford.edu

Received 4 August 2001
Published 12 October 2001

Abstract. This paper presents a combination of theory and simulation on coastal upwelling with the aim of understanding the origin and nature of the structures found. Cyclones/anti-cyclones and thin filaments observed in satellite infrared images in upwelling regions are rather well reproduced. The instabilities are confirmed to be of mixed baroclinic–barotropic and modified Rayleigh–Taylor types. Nonlinear interactions limit the growth of the large scale structures and generate 'fish-hook' structures. The Rayleigh–Taylor and mixed instabilities and fish-hook structures cause sharp increases in mixing. Mixing and stirring are quantified using a mixedness parameter and energy budgets.

Coastal perturbations modify the coherent structures which travel in the windward direction, changing their structure. The mechanisms of generation of these structures has been studied with simplified models but is not completely understood. We present animations derived from the simulations to investigate the process of formation of cyclonic/anti-cyclonic eddies. The simulations are based on solving the Navier–Stokes (N–S) equations in generalized curvilinear coordinates. The cape produces strong vortex stretching due to the acceleration of the flow around it. The continued vortex stretching results in vortex tearing in the cape vicinity which causes greater stirring than in the no-cape flow. These processes explain observed features of laboratory experiments and the observations on the west coast of the USA. The coastal perturbation inhibits the development of these structures and produces thin filaments extending offshore and downstream of the perturbation; these are an important feature of coastal upwelling.

PACS numbers: 42.27.-i, 47.11.+j, 92.10.-c, 02.60.-x

† This article was chosen from selected Proceedings of the Second International Symposium on Turbulence and Shear Flow Phenomena (KTH-Stockholm, 27–29 June 2001) ed E Lindborg, A Johansson, J Eaton, J Humphrey, N Kasagi, M Leschziner and M Sommerfeld.

 PII: S1468-5248(01)29221-2 1468-5248/01/000001+23$30.00

Contents

1. Introduction

On the eastern boundaries of oceans, circulation is strongly influenced by coastal upwelling, a phenomenon in which buoyancy, rotation, stratification and surface forcing are all significant. It is mainly due to surface forcing by the wind. On the west coast of the USA it occurs in spring and summer. In the Northern Hemisphere, atmospheric high pressure areas cause winds blowing in a southerly direction and create a current. The Earth's rotation draws this current away from the coastline. The offshore transport in the upper layer is compensated for by deep water upwelling. Figure 1 is a schematic of a typical isopycnal in a laboratory simulation of this flow. The upwelling front is where the cold, near-shore water and the warmer offshore water meet. This front undergoes instability that creates meanders.

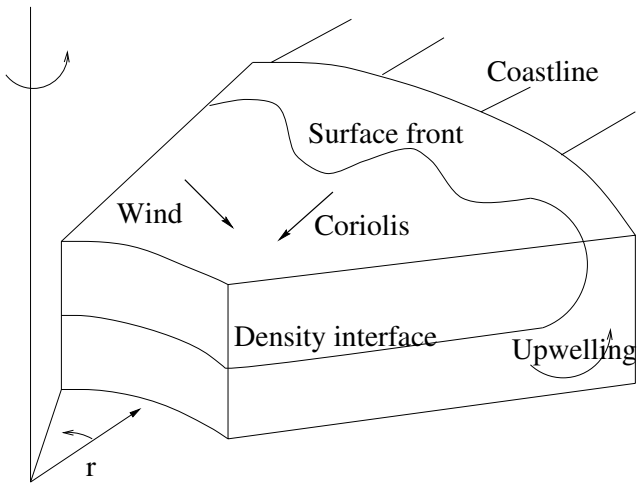

Figure 1. Schematic diagram of the upwelling process.

Laboratory experiments designed to study coastal upwelling flow have been conducted [1, 2, 3, 4]. Narimousa and Maxworthy [1] created a two-layer stratified fluid in a rotating cone-cylinder tank; hereafter, we abbreviate Narimousa and Maxworthy as NM. The top disk was rotated differentially with respect to the system rotation to simulate a surface wind stress. As a result, the density interface elevated near the outer wall and, when the surface stress was strong enough, the interface intersected the surface and formed a front that migrated offshore. The front was unstable under certain conditions and azimuthal waves appeared and grew to large amplitude. Using flow visualization, NM observed plumes, jets, and pinched-off cyclones near the front. They also studied the effects of bottom topography [1] and coastline perturbation [4] and observed several important features. When a cape was present, the first sign of upwelling always occurred adjacent to its upstream side and standing waves were found downstream. The relative importance of coastal topographic features such as capes, bathymetry and wind stress in generating the instabilities in the upwelling regions remains unclear [5, 6].

Numerical simulation can be used together with analytical modelling and laboratory experiments in the study of the coastal ocean. Zang and Street [7, 8] used large eddy simulations (LES) to study a configuration similar to that of the laboratory experiments of NM [4]. In this paper, we use an extended version of this model to study the influence of coastal perturbations on upwelling. We focus on the formation of the cyclonic/anti-cyclonic eddies generated by the instability. As upwelling is a three-dimensional process, interactions among the vortices are complex and irregular. The vortex structures are shown to be quite complicated. The formation of the filaments or strong offshore jets provides an efficient mechanism for exchange between the shelf and the deep ocean. The fish-hook structures observed in the laboratory probably have the same origin as the off-shore filaments. It is found that the Rayleigh–Taylor and mixed instabilities and fish-hook structures cause a sharp increase in mixing. A mixedness parameter and energy budgets are used to quantify mixing in the current study. An efficient method for calculating available potential energy using probability density function (pdf) is applied in the energy budget analysis [9].

This paper is organized as follows. Section 2 briefly describes the numerical simulation. Section 3 investigates the formation of the eddies. Section 4 presents the influence of a coastal perturbation on the instabilities and features such as fish-hook structures due to them. Section 5 quantifies turbulent mixing in the upwelling flow and investigates the effects of the presence of a cape on it. Finally, conclusions are given in section 6.

2. Description of the numerical simulations of upwelling

Large eddy simulation is employed to simulate the upwelling experiments of NM [4] with and without a cape. The main advantage of this approach over a hydrostatic model is that all the dynamics are included. In this section, we introduce the governing equations and numerical formulation briefly and describe the cape geometry.

2.1. Governing equations and numerical formulation

Density varies only by about a few per cent in the ocean. Hence, we may employ the Boussinesq approximation and the governing equations express mass, momentum and scalar conservation:

$$\frac{\partial u_j}{\partial x_j} = 0 \tag{1}$$

$$\frac{\partial u_i}{\partial t} + \frac{\partial F_{ij}}{\partial x_j} = S_i \tag{2}$$

$$\frac{\partial \rho_*}{\partial t} + \frac{\partial R_j}{\partial x_j} = 0 \tag{3}$$

where the fluxes and sources are

$$F_{ij} = u_i u_j + p\delta_{ij} - \nu \frac{\partial u_i}{\partial x_j} \tag{4}$$

$$S_i = -(\rho_* - \rho_b) g \delta_{i3} + 2\Omega(u_2 \delta_{i1} - u_1 \delta_{2i}) \tag{5}$$

$$R_j = u_j \rho_* - k \frac{\partial \rho_*}{\partial x_j}. \tag{6}$$

Here $\rho_* = (\rho - \rho_0)/\rho_0$ is the relative density, $\nu = \mu/\rho_0$ is the kinematic viscosity, ρ_0 is the reference density and repeated indices denote summation. The relative density is decomposed into a background density field ($\rho_b = \rho_b(x_3)$) and a perturbation density i.e. $\rho_* = \rho_b + \rho'$. Rather than the ocean, we shall simulate the laboratory experiments of NM [1, 3, 4] in which the wind stress is simulated by rotating the top lid relative to the tank at angular velocity $\Delta\Omega = 2\pi/\Delta T$, where ΔT is the rotation period of the lid. Hence, at the top of the domain, the azimuthal velocity is $u_h = -\triangle\Omega \times r$. A no-slip condition is used for the tangential velocity while the normal velocity is zero on the top, side, and bottom walls. Periodic boundary conditions are used for the flow in the azimuthal (long-shore) direction. In the initial condition the fluid is 'two-layer' stratified and the density field is horizontally uniform.

The N–S equations are solved using a finite-volume technique. The equations for the resolved field are obtained by filtering equations (1), (2) and (3). The filtered equations are transformed into curvilinear coordinates but the Cartesian velocity components are retained.

The method of fractional steps (a variant of the projection method), which splits the numerical operators and enforces continuity [10] by solving a pressure Poisson equation, is employed here. All spatial derivatives are discretized using central differences with the exception of convective terms. These terms are discretized using QUICK [11] in which the velocity components on the cell faces are computed from the nodal values using a quadratic interpolation scheme. The convective terms in the scalar transport equation are discretized using SHARP [12], a monotonic approximation that has the ability to deal with convectively dominated flows. The grid resolution studies were performed in Tadepalli [13] to validate the results and the minimum resolution required. The wave numbers obtained compare well with the linear stability analysis and laboratory experiments, while most dissipative schemes may suppress the growth of the instability and produce inaccurate stress. The momentum equations are solved using approximate factorization [14]. Details of the method can be found in Zang [7] and Tadepalli *et al* [15].

2.2. The subfilter scale model

This flow contains a wide range of scales, making it prohibitively expensive to simulate all of the scales. Hence the idea of simulating the large scale structures and modelling the small scales is very attractive. Smagorinsky [16] suggested a sub-filter scale (SFS) model in which the SFS stress is proportional to the resolved strain rate. The term 'sub-filter scale' is preferred to 'sub-grid scale' as the filter size should be greater than the grid size. This model exhibits incorrect asymptotic behaviour near boundaries, does not allow backscatter, is too dissipative for wall-bounded transitional flows [17], and correlates poorly with DNS results in homogeneous turbulence [18]. Germano *et al* [19] and Lilly [20] introduced a dynamic SFS model that predicts the correct asymptotic behaviour near the boundaries and allows energy backscatter. It has been successfully used for transitional and turbulent channel flows [19], isotropic turbulence [21] and other flows. We use the dynamic subfilter scale model with local averaging for computing the influence of small scales in the upwelling flow. The details are given in Zang [7].

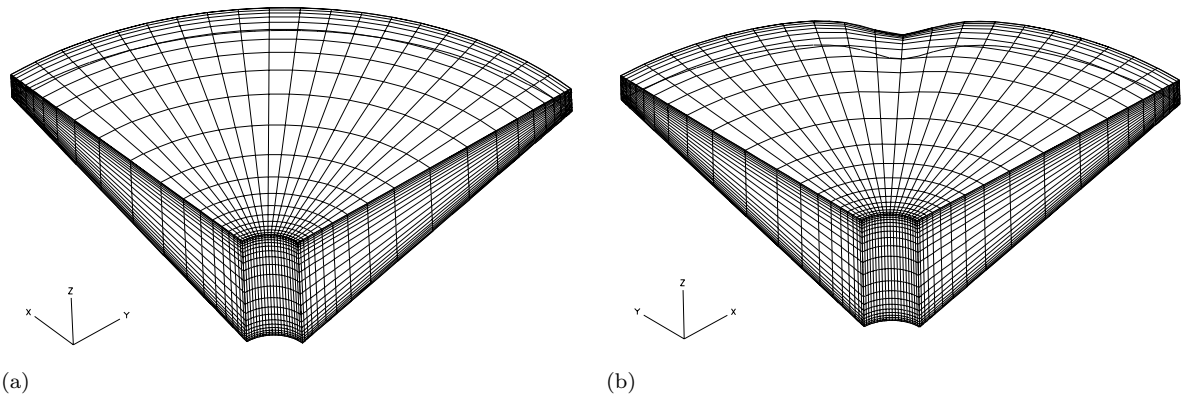

(a) (b)

Figure 2. (a) Grid for numerical simulation of upwelling flow. (b) The grid for numerical simulation with cape. (Every fourth grid is shown.)

2.3. Description of the simulations

We conducted two sets of simulations, one with and one without coastline perturbations. We will give the parameters for both simulations here. One quadrant of the tank is simulated using periodic boundary conditions in the azimuthal direction. The domain is an annular region with a sloping bottom (see figure 2 for a typical grid). The filtered Navier–Stokes equations are solved in the rotating frame. The initial vertical density distribution has a hyperbolic tangent profile approximating the two layer structure in the experiments. There is no initial azimuthal or horizontal density variation. No detailed experimental observations are available on the initial interface thickness or density distribution.

The geometry for the simulations with a cape is obtained from the function defined as 'Witch of Agnesi' [22] which relates the radial excursion distance to the azimuthal angle:

$$d(\theta) = \frac{D_c}{\beta}\left(\frac{1}{(\theta-\theta_0)^2 R_1^2 + \alpha^2} - \frac{1}{\theta_0^2 R_1^2 + \alpha^2}\right) \tag{7}$$

$$\beta = \frac{1}{\alpha^2} - \frac{1}{\theta_0^2 R_1^2 + \alpha^2} \tag{8}$$

where $d(\theta)$ is the radial excursion distance and has a maximum at $\theta = 45°$ (figure 2(b)). The parameters of the simulation are given in tables 1 and 2. The cape geometry defined above is slightly different from the cylinder of radius R_c used in the laboratory experiments of NM [4]. However, the maximum width of the cape is chosen as the cape radius (R_c) in their experiments (case: cape M) which was designed to be representative of the coastline perturbations. Since we employ periodic boundary conditions in the azimuthal direction [8], these simulations are representative of an upwelling flow with four capes, one in each quadrant. The boundary conditions were described above.

Algebraic stretching is employed to control the grid spacing to allow resolution of the boundary layers on the inner and outer boundaries of the tank. An exponentially damped stretching function ($e^{-9(i-N)^2/N^2}$, N = number of grid points in the radial direction) is used to avoid large deformations of the grid cells in the interior of the domain, which can deteriorate solution accuracy (figure 2).

The parameters of the simulations are matched to those in the experiments of NM [4, 23] and are given in table 1. The Reynolds number ($Re = \rho U_p R_0/\mu$ where U_p the disk edge velocity, R_0 the outer radius of the annulus, ρ the density and μ the viscosity of water) of

Table 1. Parameters of the simulations [23].

Tank rotation Ω (s^{-1})	2.27
Lid rotation $\Delta\Omega$ (s^{-1})	0.185
Total depth H (m)	0.20
Density diff. $\Delta\rho$ (kg m^{-3})	18
Tank radius R_0 (m)	0.45
Slope	0.27
Reynolds number Re	2995
Schmidt number Sc	723

Table 2. Parameters of the cape geometry.

α	D_c (m)	θ_0	R_c (m)	R_1 (m)
0.08	2.8E-04	45°	4.5E-2	4.5E-1

JoT 2 (2001) 014

the simulations must be lower than that of the experiments for computational efficiency. This is permitted because the flow behaviour becomes independent of Re when the latter is large enough and because the dominant instability mechanisms are inviscid. Other non-dimensional parameters include the Rossby number and the layer Froude numbers. The Rossby number is $Ro = U_p/f(R_0 - R_1)$, where U_p is the maximum lid velocity and is of the order of $O(10^{-2})$. The layer Froude numbers are defined as $f^2\lambda_s^2/g'h_{10}$ where λ_s is the theoretical stationary width of the density front, $g' = g\Delta\rho/\rho_1$ is the reduced gravity and h_{10} is the initial upper layer depth. The spin-up time [24], used as the reference time scale, is $t_s = (h_{10}/\Delta\Omega)((\Omega + \Delta\Omega)/\nu)^{1/2}$ where $\Delta\Omega$ is the differential lid angular velocity and Ω is the tank rotation angular velocity.

3. The formation of coherent structures

Tadepalli *et al* [15] applied linear stability theory (LST) to the upwelled surface front and compared the results with the experiments of NM [4]. They found the instability to be of mixed type but predominantly baroclinic. An early weak Rayleigh–Taylor (R–T) instability modifies the surface front. Although the instability mechanisms were identified, the structures are nonlinear and more complicated than those predicted by LST. The instability mechanisms play important roles in the development of the flow. Computer animation of the evolution derived from the numerical simulation provides insight into the nature of the instability. The coherent structures produced can be explored in this way.

When the top lid rotates anti-cyclonically relative to the cyclonically rotating fluid, fluid near the top surface is driven radially inward by the Coriolis force, creating the top Ekman boundary layer. Heavy fluid moves toward the outer wall and upward to replace it. When heavy fluid finally overlies light fluid, a weak modified R–T instability occurs both near the outer wall and closer to the centre. This process, together with Ekman pumping, causes a cross-shore circulation in the radial–vertical plane that has azimuthal vorticity associated with it. This vorticity can be seen in an isosurface plot (ω_θ) in figure 3(a); the isosurface shown corresponds to $\omega_\theta = 0.8U_p/D$ where D is the diameter of the domain. Figure 3 is a snapshot taken from the animation of azimuthal vorticity (animation 1). The animation goes from $t = 0.64t_s$ to $t = 3.5t_s$. Initially, the azimuthal vorticity appears near the outer boundary. It then moves away from the wall as the flow adjusts towards geostrophic balance. The wave-bands found near the centre are

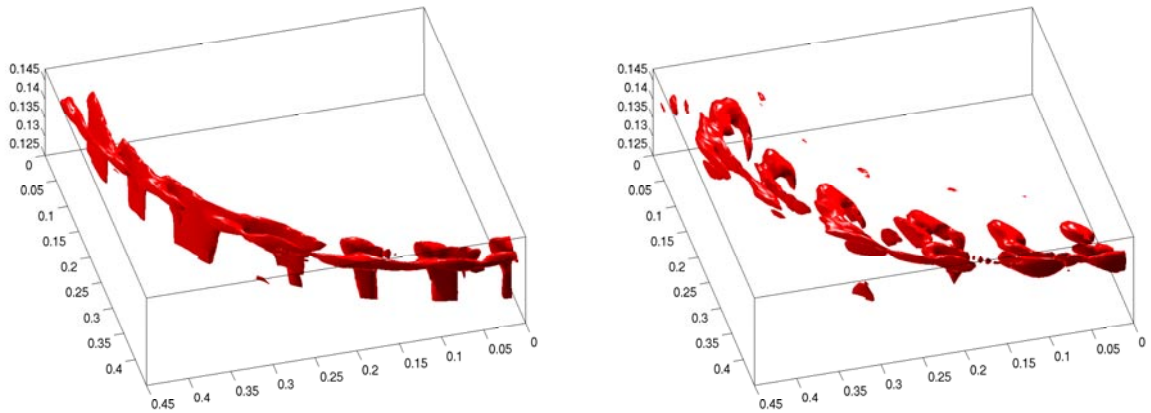

(a) (b)

Figure 3. Azimuthal vorticity in the neighbourhood of the primary front. The $\omega_\theta = 0.8U_p/D$ isosurface is shown at (a) $t = 1.12t_s$, (b) $t = 1.34t_s$.

much less energetic than the baroclinic–barotropic (B–B) instability mode that occurs later [15]. An intensive mixing zone then develops between the surface front and the coast. The mixing and friction reduce the azimuthal vorticity near the wall (figure 3(b) and animation 1).

At this stage, the vertical vorticity (ω_z) in the vicinity of surface front is essentially a vortex sheet (figure 4(a)). The folding that follows is very sensitive to small perturbations. As the disturbance grows, it quickly takes on a more B–B character. Small amplitude azimuthal waves first appear at the primary front. They develop into a series of cyclones and anti-cyclones. Cyclonic eddies are usually found at the front while anti-cyclonic eddies are found closer to the wall. The cyclonic eddies often pinch off from the front to form isolated vortices. In the current simulation six isolated vortices form as predicted by LST and seen in the laboratory experiments [15, 4]; see figure 4(c) and (d)). We trace the cyclonic eddies via an isosurface with $\omega_z = 1.1U_p/D$. The isolated vortices move off-shore slowly and then decay (figure 4(e) and (f)).

The B–B instability produces quasi-horizontal convection that is best visualized in two dimensions. These azimuthal frontal waves are observed often in satellite infrared (IR) images during the upwelling season. The formation of these large scale structures could also be associated with coastal geometry or bottom topography [6, 25]. Top view animations of the vorticity and the density field at $z = 0.93h$ are found in animations 2 and 3. Also, a few thin filaments of heavy fluid are observed to move offshore after $t = 2t_s$ in the density animation. The details of these events depend strongly on the initial perturbations. The animation starts at t=$0.8t_s$ and no coastal perturbation is present in it. Coastal geometry effects will be discussed in next section.

The 3D isosurfaces of vertical vorticity shown in figure 4 demonstrate the formation of eddies ($t = 0.94t_s$ to $t = 1.68t_s$). The two-dimensional animations (2 and 3) also illustrate the eddy formations and represent the vertical vorticity field quite well. However, recall that the mechanisms are three-dimensional and involve vortex stretching. These are demonstrated in the isosurface plot of azimuthal vorticity and the vertical vorticity animations (1, 2 and 3). This can be found in the later stages of animation 1 in which the azimuthal vorticity is growing and elongated and may be due to the susceptibility of the quasi-two dimensional vortices to secondary instability. If a vortex develops a slight kink due to small perturbation, the velocity field it induces lifts or lowers the kink. This process is very effective in stretching vortices. The effect of the vortex stretching can also be seen in animations 2 and 3. A great deal of

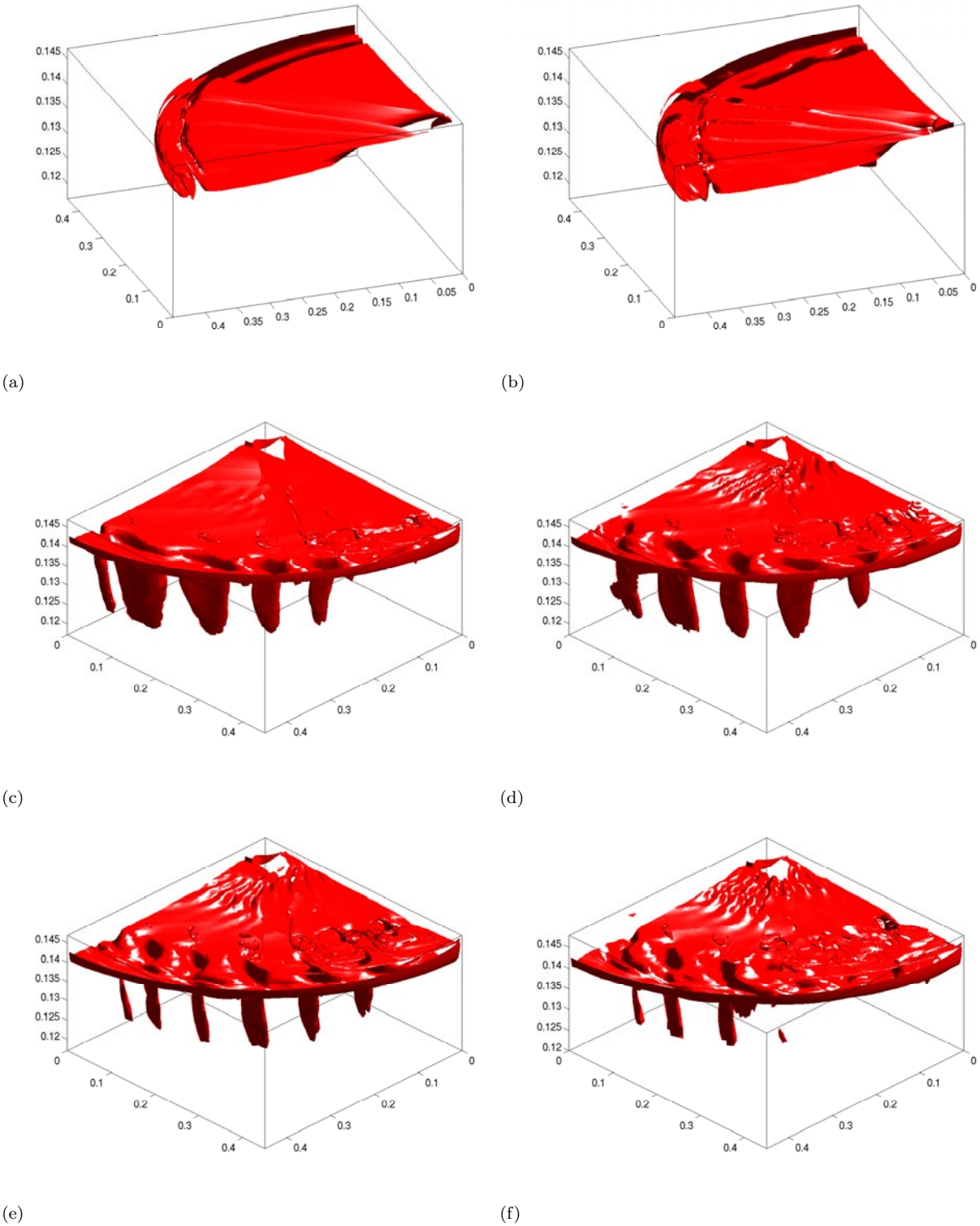

Figure 4. Vertical vorticity in the neighbourhood of the primary front. The $\omega_z = 1$ isosurface is shown at (a) $t = 0.94t_s$, (b) $t = 1.02t_s$, (c) $t = 1.14t_s$, (d) $t = 1.32t_s$, (e) $t = 1.50t_s$, (f) $t = 1.68t_s$.

turbulence production takes place by vortex stretching. In the current simulation with a well-defined coastline, the filaments may develop into the fish-hook structures seen in the laboratory. Because a still wider variety of processes can take place in this complicated tangle of vortices, this three-dimensional flow is more sensitive to small disturbances than the earlier stages of the flow.

4. The effects of coastal perturbations on the large scale structure

Coastline perturbations and topography [26, 27, 28] play a significant role in the dynamics of coastal currents and fronts and produce some of the features observed in the satellite infrared images. Topographic features such as capes and ridges [29] have a profound influence on the large-scale features. However, the mechanisms are not understood in detail. In this section, we explore the large-scale structures and quantify the influence of a coastal perturbation using animations 1–3 (without a cape) and 4–6 (with a cape).

4.1. Modification of instabilities with coastal perturbations

Animation 4 uses the same isosurface value as animation 1 to show the the evolution of the azimuthal vorticity in the case with with coastal perturbation. Animations 5 and 6 give two-dimensional views of the vertical vorticity and density at the same horizontal location as animations 2 and 3. The vertical and azimuthal vorticities shown in animations 4–6 are both larger and more irregular than those in animations 1–3. We stretched the colour-map results using a square root factor in order to cover the whole vorticity range. The maximum vertical vorticity in animations 4–6 is about three times of the maximum value in animations 1–3 ($\omega_{z_{max}} \approx 20U_p/D$ in 4–6 compared with $\omega_z \approx 6U_p/D$ in 1–3). The maximum occurs in the vicinity of the cape.

Figure 5 compares snapshots taken from the animations of the scalar field with and without the coastline perturbation at $z = 0.93h$ at $t = 1.12t_s$. During the initial upwelling, the primary front is drawn closer to the 'coastline' on the downstream side of the cape. The front downstream of the cape is wider than the no-cape front (figure 5). Contour plots of the vertical vorticity at the same horizontal sections are shown in figure 6. In the simulation with a cape, the vorticity field is more irregular and the strongest vorticity is located near the cape rather than being spread over the whole side boundary. A large perturbation in the azimuthal velocity is observed just downstream of the cape as shown by the enlarged velocity vector plot in figure 7. Very strong recirculation occurs adjacent to the back of the cape and coincides with the separation zone.

NM [4] indicated that baroclinic waves interact with standing waves on the downstream side of the cape. Their observations were based on visual examination of the features observed in the experiments but no quantitative measurements were made to confirm the existence of the standing waves. The current simulations (similar to case:M of their experiments) suggest that the waves on the surface front are the result of mixed baroclinic–barotropic instability and move in the direction of the surface forcing (clockwise) in the rotating frame (animation 6). The major difference between our simulations and NM's experiments is the value of disk friction velocity ($u_* = \sqrt{\tau_w/\rho}$) so that there is significant difference in the nondimensional parameter $\theta_* = g'h_{10}/u_* f\lambda_s$ shown by NM to be an important parameter for determining stability and the size and drift velocity of the baroclinic waves in coastal upwelling. We obtain u_* from the surface shear stress at the disk which has been verified by the grid resolution studies [30]. However, NM inferred u_* from an analysis of previous experiments. θ_* is the combination of Rossby radius normalized by λ_s and Richardson number ($\theta_* = \sigma Ri^{1/2}$) from [1]. $\sigma = \sqrt{g'h_{10}}/f\lambda_s$ is the

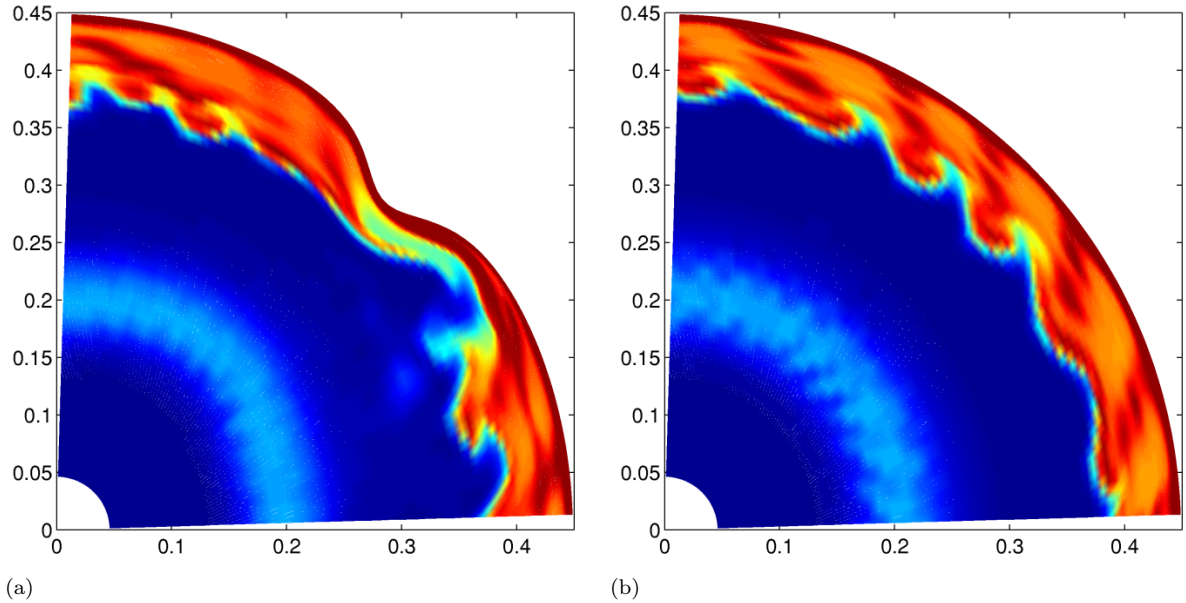

Figure 5. Density field in the neighbourhood of the primary front with (a) and without (b) the coastline perturbation at $t = 1.12t_s$ and $z = 0.93h$.

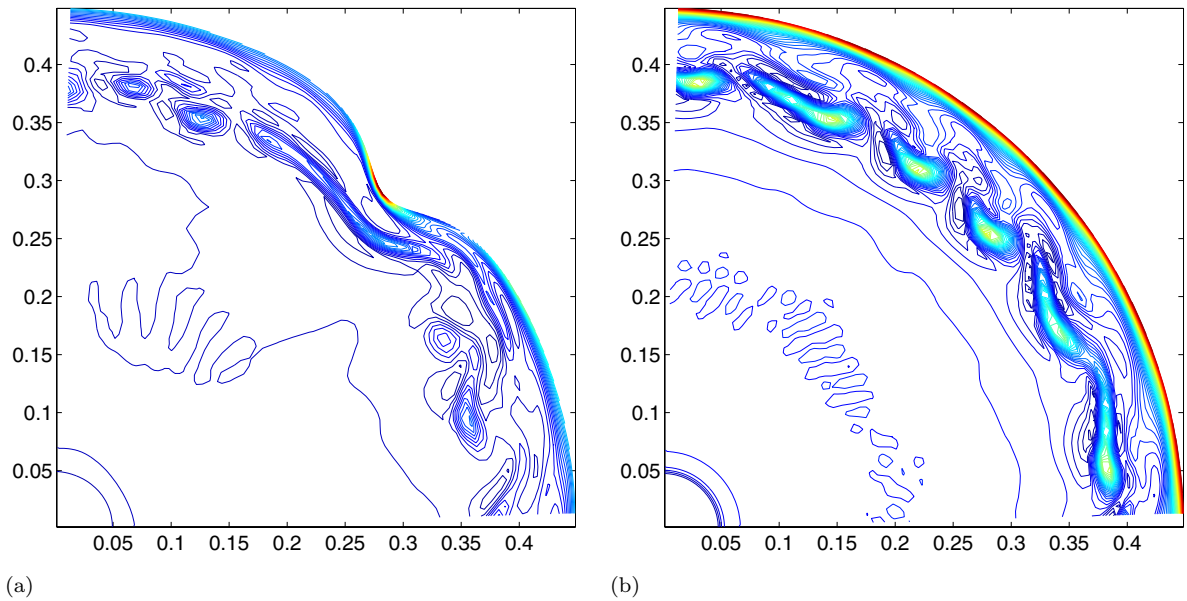

Figure 6. Vertical vorticity in the neighbourhood of the primary front with (a) and without (b) the coastline perturbation at $t = 1.12t_s$ and $z = 0.93h$.

'Rossby/Froude' number defined in [31] for two-layer stratified flow (horizontal length scale is normalized by λ_s), which is used commonly in the baroclinic instability criteria. $Ri = g'h_{10}/u_*^2$ represents the stratification forcing governing the size and drift velocity of the baroclinic waves. The flow becomes unstable as θ_* decreases. θ_* in our simulation is $\theta_* = 1.12$ which is smaller than the lowest value of θ_* ($\theta_* \approx 2$) in NM. They mainly focused on the cases in which a stable standing wave existed. The standing wave usually became unstable later and propagated

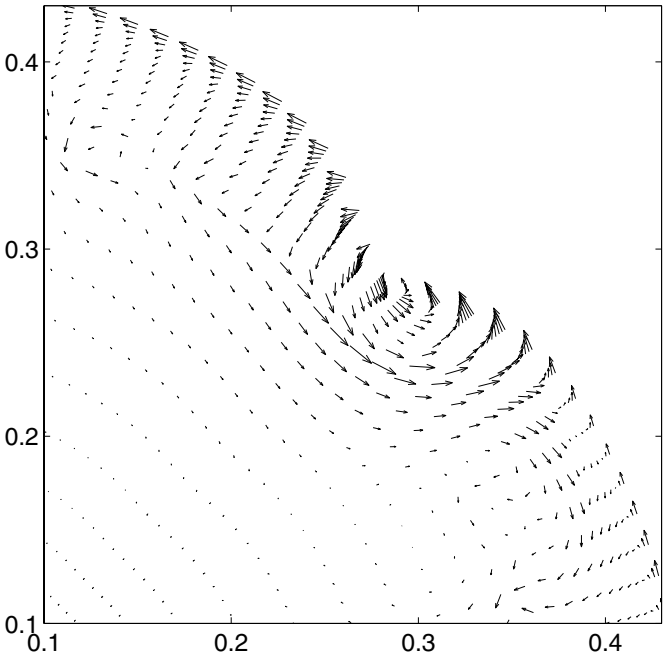

Figure 7. Horizontal velocity vectors near the perturbated coastline at $t = t_s$ and $z = 0.93h$. (Every second grid is shown and the reference frame is travelling with the frontal waves).

in the offshore direction for small θ_*. Eventually, a cyclone pinched off. These observations are reproduced in our simulations. The animation shows the formation of the first baroclinic wave, which is the largest and most significant one [13]. It forms downstream of the cape [4]. The baroclinic waves are modified by the cape, mainly in the troughs (which are closer to the 'coastline'). The front excursions are more irregular (figure 8) than those without the cape. In the latter case, they are nearly periodic as seen in animation 3.

The mechanism of the formation process can be explained in terms of vortex stretching. The front excursions are caused by the presence of large-scale vortices. The vortices are elongated by the strain caused by the cape (figure 9). Trace the vortex 'A' in figures 8 and 9. As it moves clockwise, it is stretched by the strain produced by the acceleration of the fluid passing the cape. Figure 9 shows the absolute vertical vorticity at the same times as in figure 8. As the flow evolves, the surface front (figure 8) meanderings increase, causing distortion of the density front. All the vortices are elongated as they have already moved past a cape. (Recall that the periodicity implies that there are four capes.) The increased stretching of the front results in increased mixing and increase the strength of azimuthal vorticity (animation 4), particularly in the vicinity of the cape. Strong azimuthal vorticity is always found just downstream of the cape. The dynamics can be described in terms of the vertical vorticity. Continued stretching results in tearing of the vortex (figure 9). This simulation provides a quantitative explanation for the results observed by NM [4] with a coastal perturbation. Figure 8 also shows the creation of a diverging flow just downstream of the cape, which provides a possible mechanism for the production of long, thin offshore filaments of upwelled water observed in the ocean. The flow divergence causes the upwelled water to advect in the offshore direction.

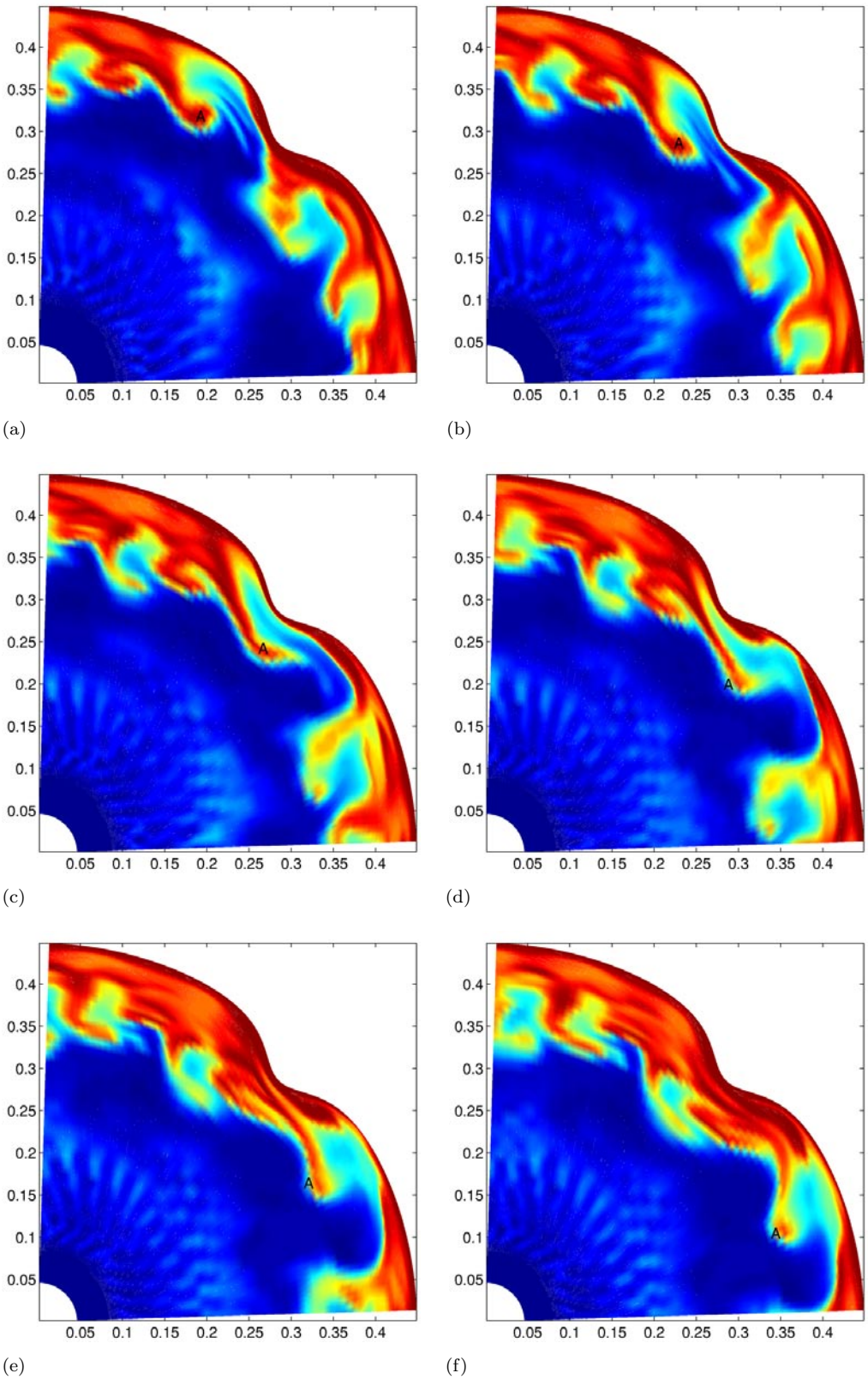

Figure 8. Density field with coastal perturbation in the neighbourhood of the primary front at (a) $t = 1.38t_s$, (b) $t = 1.41t_s$, (c) $t = 1.44t_s$, (d) $t = 1.47t_s$, (e) $t = 1.51t_s$, (f) $t = 1.54t_s$ at $z = 0.93h$.

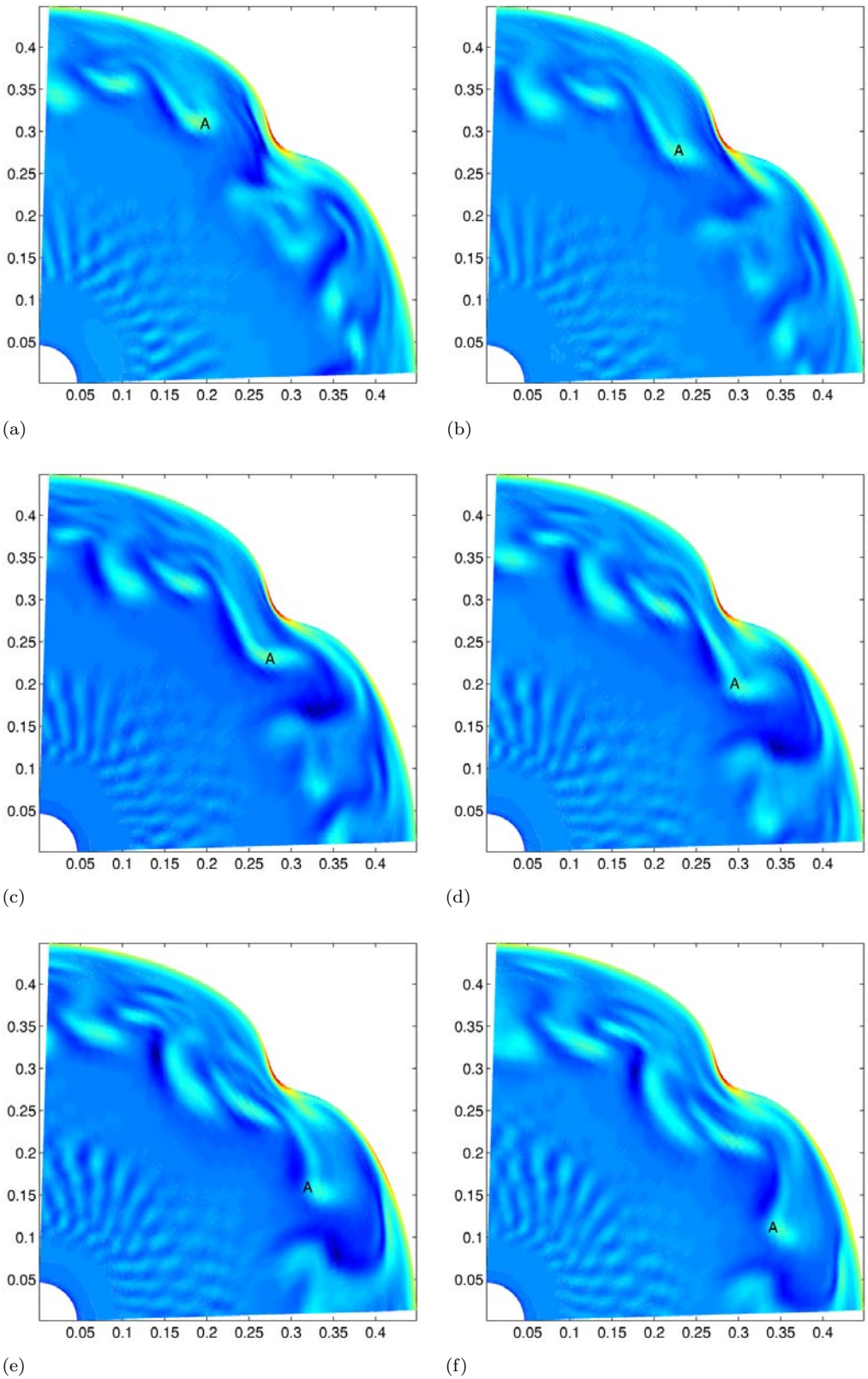

Figure 9. Vertical vorticity with coastal perturbation in the neighbourhood of the primary front. (a) $t = 1.38t_s$, (b) $t = 1.41t_s$, (c) $t = 1.44t_s$, (d) $t = 1.47t_s$, (e) $t = 1.51t_s$, (f) $t = 1.54t_s$ at $z = 0.93h$.

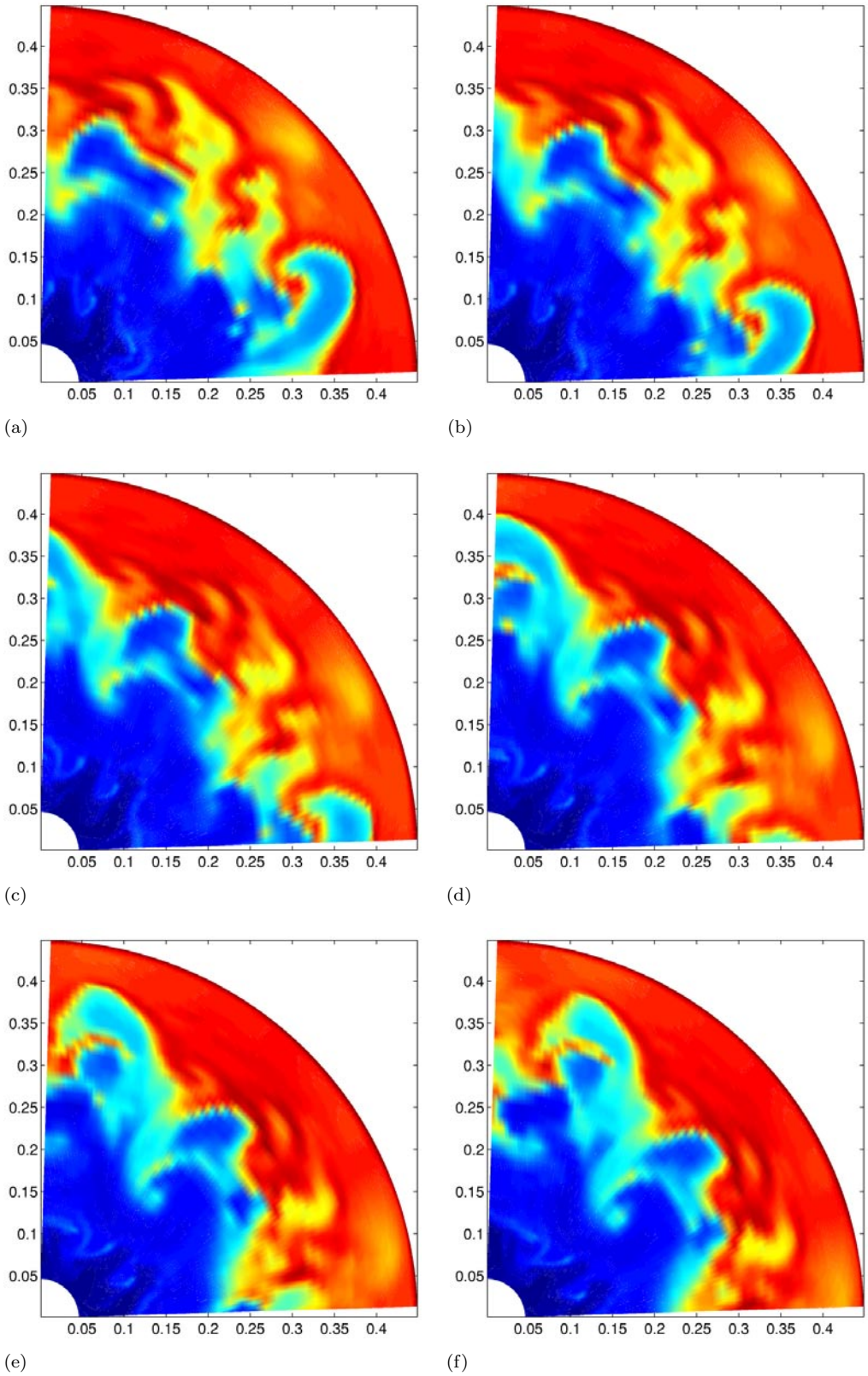

Figure 10. Density field at $z = 0.93h$, $t = 3.67t_s$ (a), $3.70t_s$ (b), $3.73t_s$ (c), $3.77t_s$ (d), $3.80t_s$ (e), $3.83t_s$ (f).

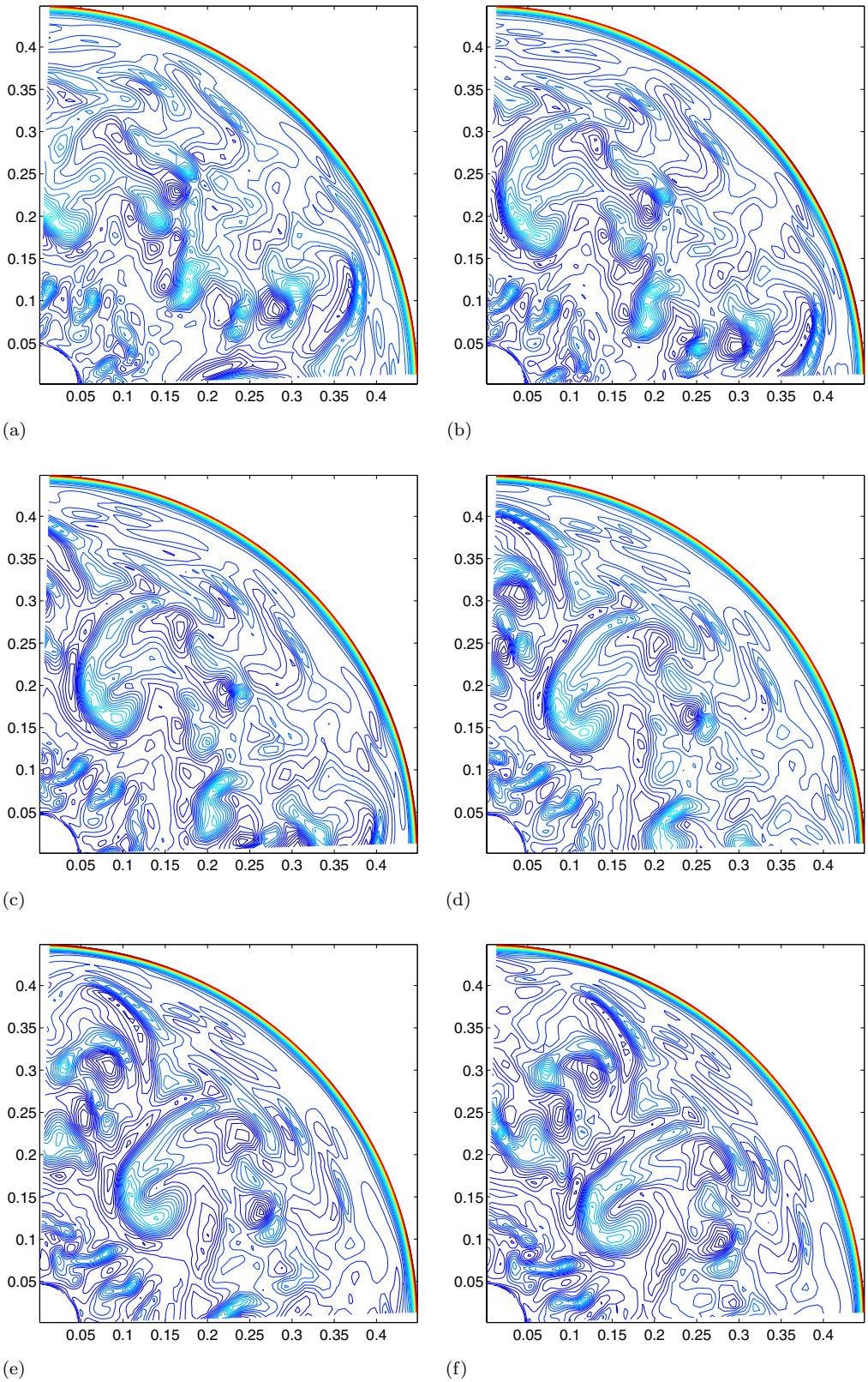

Figure 11. Relative vorticity field at $z = 0.93h$, $t = 3.67t_s$ (a), $3.70t_s$ (b), $3.73t_s$ (c), $3.77t_s$ (d), $3.80t_s$ (e), $3.83t_s$ (f). Dark lines indicate negative relative vertical vorticity (clockwise).

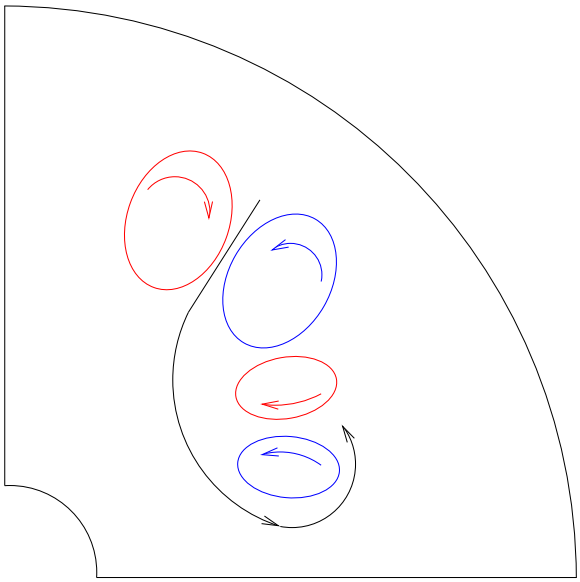

Figure 12. The possible mechanism of formation of the fish-hook structures.

4.2. Fish-hook structures

A great deal of alongshore variability of the large meanders is observed in satellite measurements. Strong winds can break these meanders, forming detached eddies that have been observed off the west coast of the USA [32]. The laboratory experiments of NM [23, 4] reproduced many of these features. Upwelling filaments are the most prominent features; however, the generation mechanism is still unclear. Their origins are highly correlated to the fish-hook structure observed in the laboratory and in the current simulation [13].

Nonlinear interactions that moderate the growth of the large-scale structures become important when the density front becomes highly non-axisymmetric (when $t > 3t_s$). Fish-hook structures are a by-product of these nonlinear interactions and originate from the modulation of the large-scale structures [13]. Some vortices grow in size at the cost of others. As a result, eddies of different sizes are observed. Figure 10(a)–(f) shows a pair of counter-rotating vortices that pump upwelled high density fluid from the outer edge of the tank towards the centre. The corresponding contours of relative vertical vorticity are shown in figure 11 and confirm the presence of elongated vortical structures created by the pumping action. As the fluid has different velocity from the local fluid, it moves relative to it, producing the fish-hook. The angle of the fish-hook is governed by a second, relatively weak, pair of counter-rotating vortices that draws the fluid ejected by the first pair of vortices back towards the coast. In figures 10(e), (f), we see another fish-hook structure that was formed upstream with different strength. The strength of the fish-hook structure grows as time evolves (animation 3).

A schematic of the process is given in figure 12. The fish-hook structures are advected in the lid rotation direction (clockwise) as is evident in the sequence in figure 10. Figure 13 shows the scalar field at four different heights, indicating that these structures are not two-dimensional; their intensity decreases with depth. The front excursion due to the fish-hook grows, trapping a pocket of low density fluid as seen in figure 14. This suggests a possible mechanism for production of isolated pockets seen in the ocean. This process causes considerable horizontal and vertical mixing. In the presence of a cape, the fish-hook structure is less pronounced. In its place, there are more thin filaments of a kind frequently observed in coastal regions.

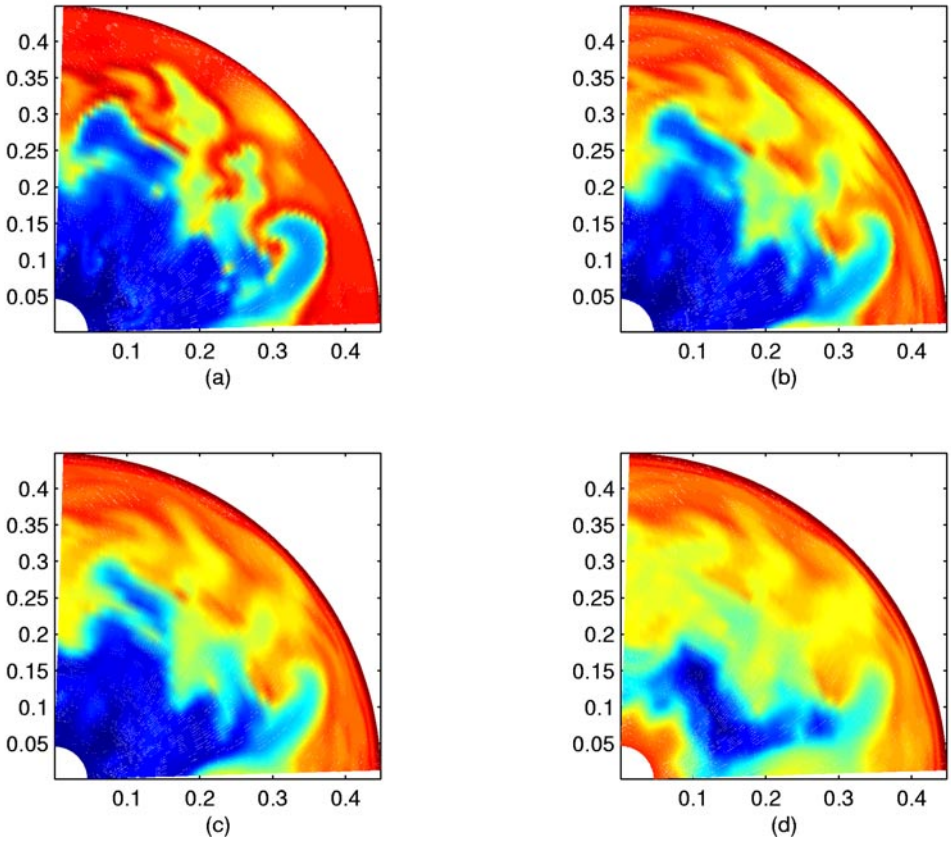

Figure 13. Horizontal sections of the scalar field at $t = 3.9t_s$ indicating the fish-hooks for $z =$ (a)$0.93h$, (b)$0.86h$, (c)$0.72h$, (d)$0.50h$.

5. Mixing in upwelling flows

As noted above, it is widely believed that coastline perturbations and topography have a significant effect on coastal currents, fronts and upwelling and are responsible for the major features observed in satellite infrared (IR) images [27] and enhanced mixing. In this section, we will concentrate on the mixing events occurring in the simulation.

It is important to distinguish between the processes of stirring and mixing. The former involves the bringing of fluids of different density into contact through the action of strain, which may be due to turbulence. After the fluid has been stirred, it may re-stratify through gravitational action, returning it to its original height. Mixing requires that the fluids combine at the molecular level and is an irreversible process. It is difficult to quantify mixing in either field measurements or laboratory experiments because very detailed data are required. In this study, we quantify mixing by using a mixedness parameter (M) and by computing the reference potential energy (RPE).

5.1. Mixing parameter

The mixedness parameter defined below measures the fraction of the fluid that has been mixed. This mixedness parameter M is essentially the one proposed by Roshko [33] for the mixing fluid

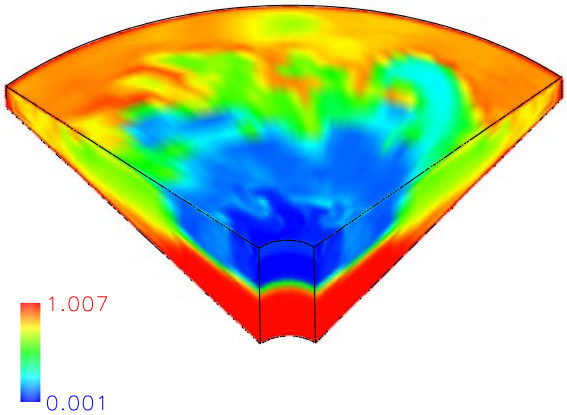

Figure 14. Three-dimensional view of the enlarged mixed region shown in the scalar field at $t = 3.67t_s$. The horizontal cut is made at $z = 0.93h$.

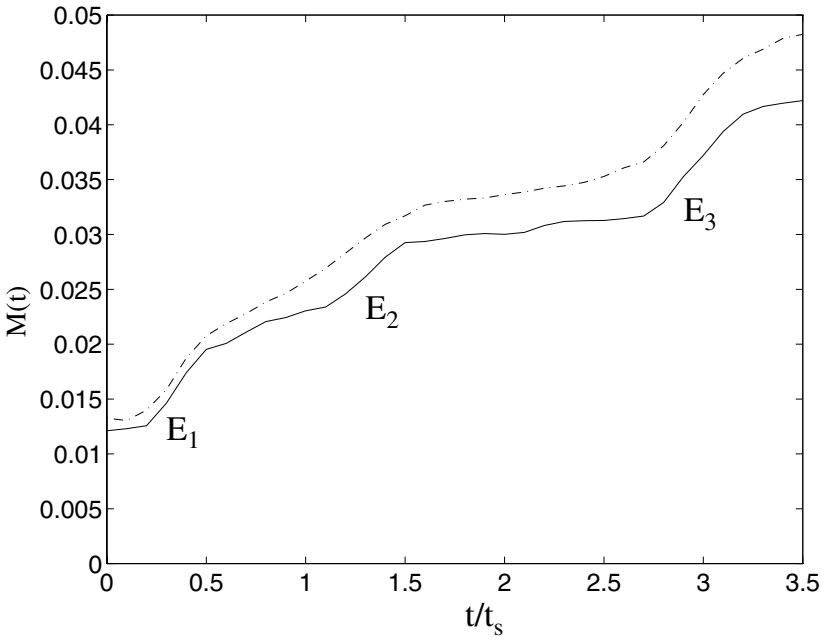

Figure 15. Mixedness parameter for upwelling flow with (chain curve) and without (full curve) coastline perturbation.

of different velocities and is defined by:

$$M(t) = \frac{1}{V}\int_V c(1-c)\mathrm{d}V = \overline{c} - \overline{c^2} \tag{9}$$

where V is the total volume of the domain, $\overline{c} = \frac{1}{V}\int_V c\mathrm{d}V$, $\overline{c^2} = \frac{1}{V}\int_V c^2\mathrm{d}V$ and $c = (\rho - \rho_0)/\Delta\rho$, ρ_m is the density of the fluid in the upper layer (the minimum density found in the flow) and $\Delta\rho = \rho_M - \rho_m$ is the density difference between the lower and upper layers. Since $0 \leq c \leq 1$, $M = 0$ and $M = 0.25$ for the completely unmixed and fully mixed situations, respectively. Figure 15 shows the evolution of the mixedness parameter in the upwelling flow with and without the cape. The observed mixedness is much smaller than 0.25, since mixing occurs only in a small

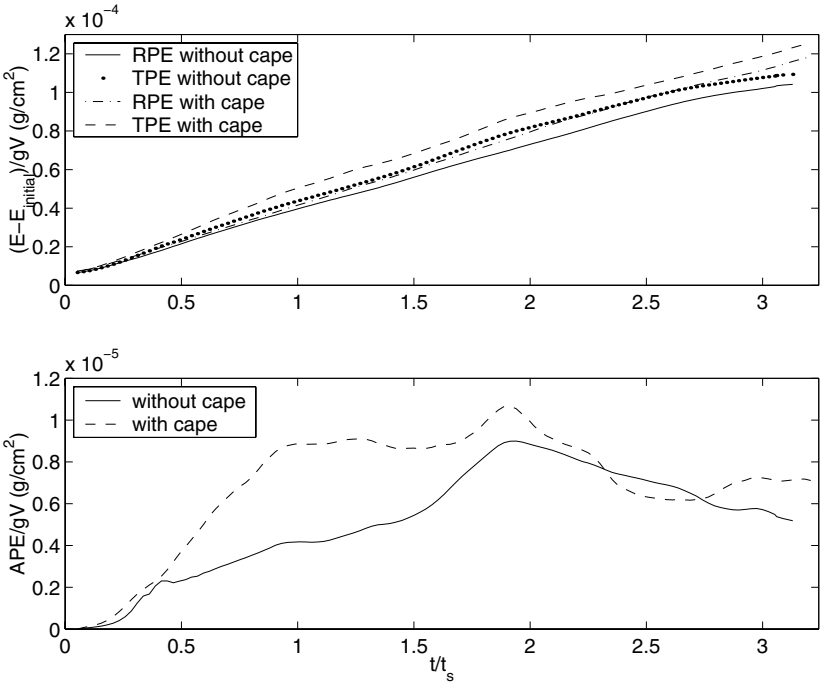

Figure 16. (a) The evolution of RPE and TPE. The initial RPE has been subtracted. (b) The evolution of APE.

portion of the flow. The amount of the mixed fluid increases monotonically with time, as it must. Greater mixing is observed in the case of cape flow due to the larger front excursions and vortex stretching described above. The sharp increase of mixing in event E_1 is due to the initial Rayleigh–Taylor instability. Event E_2 is due to the onset of the mixed-instability of the front and the event E_3 is due to the formation of the fish-hook structures.

The definition of the mixedness parameter in (9) is appropriate since its rate of change is positive definite and is proportional to the scalar dissipation χ:

$$\frac{k}{2}\mathrm{d}M/\mathrm{d}t = \frac{k}{2}\int \bigtriangledown c \cdot \bigtriangledown c \mathrm{d}V \propto \chi > 0 \tag{10}$$

where k is the diffusivity for density. This indicates that M is a monotonic function of time.

5.2. Energy budgets

The reference potential energy is a direct measure of potential energy change due to irreversible diapycnal mixing [9, 34]. Energy budgets thus provide another index for quantifying mixing. The reference potential energy state has the minimum potential energy that can be obtained through adiabatic redistribution of the density [34]. Tseng and Ferziger [9] developed an efficient approach for calculating the RPE through the probability density function (pdf). The approach requires significantly less computation than the standard approach, especially in three dimensions. We extend the pdf approach to the investigation of mixing in upwelling flow. The RPE is defined as

$$RPE = \int_{\rho_m}^{\rho_M} \rho g Z_r(\rho) \mathrm{d}\rho \tag{11}$$

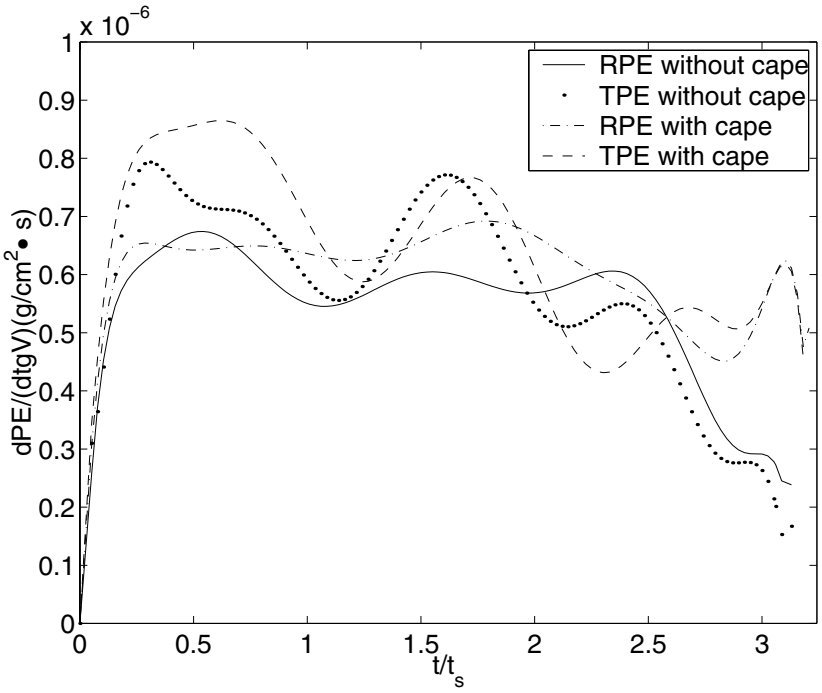

Figure 17. The instantaneous creation rate of RPE and TPE (with (chain curve) and without (broken curve) coastline perturbation).

where ρ_m and ρ_M are minimum and maximum values of the density. Z_r is the reference state of density ρ. For an arbitrary domain with complex geometry, Z_r can be obtained from

$$\int_0^{Z_r(\rho)} A(z)\mathrm{d}z = V \int_\rho^{\rho_M} P(\tilde{\rho})\mathrm{d}\tilde{\rho} \tag{12}$$

where $A(z)$ is the horizontal sectional area. $P(\tilde{\rho})$ is the probability density function of the domain V and is defined in terms of the volume integral of a delta function

$$P(\tilde{\rho}) \equiv \frac{1}{V}\int_V \delta(\tilde{\rho} - \rho)\mathrm{d}V. \tag{13}$$

Note that the reference state profile $Z_r(\rho)$ is a monotonic function of the density ρ and is dimensionally a length. Only molecular mixing can alter the pdf of density field and thus change the reference potential energy.

The evolution of the energy budgets in the cases with and without the cape is shown in figure 16. Both RPE and TPE are slightly larger in the simulation with coastal perturbation. Available potential energy (APE) is the difference between TPE and RPE. The evolution of the RPE and TPE in the two cases is quite similar. Figure 17 shows the instantaneous rate of change of RPE and TPE. There are three peaks, corresponding to the three mixing events in figure 15. The peak of the TPE growth rate at event E_3 is less than that at events E_1 and E_2 because the fish-hook generation process is more localized than the others. The increased irreversible mixing at the later stages of evolution mainly results from the increased interface area between the fluids of different density.

APE is the portion of potential energy available for conversion to kinetic energy. The cape case generates significant potential energy and thus greater global stirring as the instability (figure 16). This is as expected. The APE is primarily located at the upwelling

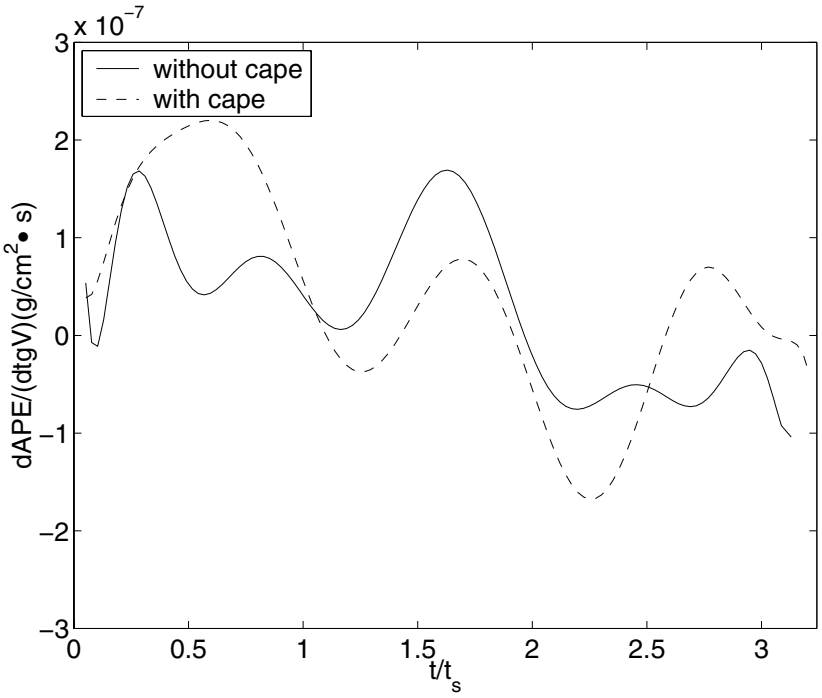

Figure 18. The instantaneous rate of APE without (full curve) and with (broken curve) coastline perturbation).

front and increases as the front migrates. Figure 18 shows the instantaneous rate of increase of the APE. The transfer between kinetic energy and available potential energy is significant when the instability occurs, implying that most of the energy involved in the upwelling process is stored as APE. Slightly greater stirring occurs in the simulation with the cape.

6. Summary and conclusion

The aim of this study was to further understand the formation of the cyclonic/anti-cyclonic eddies and the effects of coastal perturbation on the features of coastal upwelling. To accomplish this, we performed large eddy simulations of laboratory experiments with and without a small cape on the boundary. The upwelled front modification is explained in detail. The visualizations help one understand the dynamics of coherent structures as demonstrated by animations 1–6. Animations 1–3 show the generation of large-scale eddies by B–B instability. The existence of such structures explains the three-dimensional evolution of the B–B instability. The vertical vorticity is quasi-two-dimensional. The azimuthal vorticity is more complicated and is fully three-dimensional. The other animation concerns a flow past a cape. Use of various views helped to track the creation of secondary vortices.

The simulation suggests that waves on the surface front resulting from mixed B–B instability are modified by the cape and the front excursions become more irregular. The results identify several important features observed in the laboratory and the ocean. The large fish-hook structures observed in the upwelling experiments are predicted by the numerical model. They are generated by the pumping action of two pairs of counter-rotating vortices. They are responsible for both horizontal and vertical mixing.

The coastal perturbation inhibits the development of these structures and instead produces

many thin filaments extending offshore and downstream of the cape. The primary front is the most energetic region of the flow. The front is more irregular and mixing is enhanced by the presence of a cape. Strong vortex stretching is observed as a result of the acceleration around the cape. Continued vortex stretching results in vortex tearing. The large scales propagate in the downwind direction and are not phase-locked by the cape. A steep increase in the amount of mixed fluid is caused by the Rayleigh–Taylor instability, mixed baroclinic–barotropic instability and the fish-hook structures. This is shown by the mixedness parameter and energy budgets. The potential energy evolution indicates increased stirring as these instabilities occur and shows more available potential energy in mixed instability. The result agrees well with the energy spectrum analysis [15]. Interestingly, a small cape in the simulation increases the APE significantly, which implies more stirring, but does not change the RPE greatly. This is not surprising and results from the global property of reference potential energy. We believe that locally stronger stirring near the frontal modification enhances irreversible mixing near the coastal boundary.

Acknowledgments

Financial support for this work was provided by National Science Foundation High Performance Computing and Communication program, grant number DMS-9218166.

References

[1] Narimousa S and Maxworthy T 1985 Two-layer model of shear-driven coastal upwelling in the presence of bottom topography *J. Fluid Mech.* **159** 503–31
[2] Monismith S 1986 An experimental study of the upwelling response of stratified reservoirs to surface shear stress *J. Fluid Mech.* **171** 407–39
[3] Narimousa S and Maxworthy T 1987 Coastal upwelling on a sloping bottom: the formation of plumes, jets and pinched–off cyclones *J. Fluid Mech.* **176** 169–90
[4] Narimousa S and Maxworthy T 1987 On the effects of coastline perturbations on coastal currents and fronts *J. Phys. Oceanogr.* **17** 1296–303
[5] Allen J S, Newberger P A and Federiuk J 1995 Upwelling circulation of the Oregon continental shelf. Part I: Response to ideal forcing *J. Phys. Oceanogr.* **25** 1843–66
[6] Lentz S J 1995 U.S. contributions to the physical oceanography of continental shelves in the early 1990's *Rev. Geophys.* **33** 1225–36
[7] Zang Y 1993 On the development of tools for the simulation of geophysical flows *PhD Thesis* Stanford University
[8] Zang Y and Street R L 1995 Numerical simulation of coastal upwelling and interfacial instability of a rotating and stratified fluid *J. Fluid Mech.* **305** 47–75
[9] Tseng Y H and Ferziger J H 2001 Mixing and available potential energy in stratified flows *Phys. Fluids* **13** 1281–93
[10] Kim J and Moin P 1985 Application of a fractional-step method to incompressible Navier-Stokes equations *J. Comput. Phys.* **59** 308–23
[11] Leonard B P 1979 A stable and accurate convective modelling procedure based on quadratic upstream interpolation *Comput. Methods Appl. Mech. Eng.* **19** 58–98
[12] Leonard B P 1988 Simple high-accuracy resolution program for convective modeling of discontinuities *Int. J. Numer. Methods Fluids* **8** 1291–318
[13] Tadepalli S 1997 Numerical simulation and prediction of upwelling flow *PhD Thesis* Stanford University
[14] Beam R M and Warming R F 1976 An implicit finite-difference algorithm for hyperbolic systems in conservation law form *J. Comput. Phys.* **22** 87–110
[15] Tadepalli S, Ferziger J H and Tseng Y H 2001 Simulation of coastal upwelling. I: linear stability and the early turbulent regime *J. Phy. Oceanogr.* submitted
[16] Smagorinsky J 1963 General circulation experiments with the primitive equations, I. The basic experiment *Monthly Weather Rev.* **91** 99–164
[17] Piomelli U, Zang T A, Speziale C G and Hussiani M Y 1990 On the large-eddy simulation of transitional wall-bounded flows *Phys. Fluids* A **2** 257–65

[18] Bardina J, Ferziger J H and Reynolds W C 1983 Improved turbulence models based on large eddy simulation of homogeneous, incompressible, turbulent flows *Technical Report* TF-19, Thermal sciences division, Department of Mechanical Engineering, Stanford University
[19] Germano M, Piomelli U, Moin P and Cabot W H 1991 A dynamic sub-grid scale eddy viscosity model *Phys. Fluids* A **3** 1760–5
[20] Lilly D K 1992 A proposed modification of the Germano subgrid scale closure method *Phys. Fluids* A **4** 633–5
[21] Moin P, Squires K, Cabot W and Lee S 1991 A dynamic subgrid-scale model for compressible turbulence and scalar transport *Phys. Fluids* A **3** 2746–57
[22] Beyer W H 1981 *CRC Standard Mathematical Tables* 26th Edn (Boca Raton, FL: CRC Press)
[23] Narimousa S and Maxworthy T 1991 Experiments on the structure and dynamics of forced, quasi-two-dimensional turbulence *J. Fluid Mech.* **223** 113–33
[24] Linden P F and Van Heijst J F 1984 Two-layer spin-up and frontogenesis *J. Fluid Mech.* **143** 69–94
[25] Narimousa S and Maxworthy T 1989 Application of a laboratory model to the interpretation of satellite and field observations of coastal upwelling *Dyn. Atmos. Oceans* **13** 1–46
[26] Flament P, Armi L and Washburn L 1985 The evolving structure of an upwelling filament *J. Geophys. Res.* **90** 1765–985
[27] Breaker L C and Mooers C N K 1986 Oceanic variability off the central California coast *Prog. Oceanogr.* **17** 61–135
[28] Brink K H 1988 Topographic drag due to barotropic flow over the continental shelf and slope *J. Phys. Oceanogr.* **16** 2150–8
[29] Luther M E and Bane J M 1985 Mixed instabilities in the Gulf-stream over the continental slope *J. Phys. Oceanogr.* **15** 3–23
[30] Cui A 1999 On the parallel computation of turbulent rotating stratified flows *PhD Thesis* Stanford University
[31] Lesieur M, Métais O and Garnier E 2000 Baroclinic instability and severe storms *J. Turbulence* **1** 002
[32] Kosro P M 1987 Structure of the coastal current field off northern California during the coastal ocean dynamics experiment *J. Geophys. Res.* **92** 1637–54
[33] Roshko A 1976 Structure of turbulent shear flows: A new look *AIAA J.* **14** 1349–57
[34] Winters K B, Lombard P N, Riley J J and D'Asaro E A 1995 Available potential energy and mixing in density-stratified fluids *J. Fluid Mech.* **289** 115–28